PARTITIONED INVERSE IMAGE RECONSTRUCTION FOR MILLIMETER-WAVE SAR IMAGING

Sandamali Devadithya[1], *Andreas Pedross-Engel*[1], *Claire M. Watts*[1], *and Matthew S. Reynolds*[1,2]

[1]Department of Electrical Engineering, [2] Department of Computer Science and Engineering, University of Washington, 185 Stevens Way, Seattle, WA, 98195.

ABSTRACT

Synthetic aperture radar (SAR) images are representations of the microwave or millimeter-wave reflectivity of the observed scenes. SAR image reconstruction is an inverse problem, which can be solved via an approximation, e.g. matched filter (MF), or the explicit inverse using a large amount of measurement data. However, the approximation limits the resolution while the explicit inverse is computationally complex and mostly ill-conditioned. This paper proposes a partitioned inverse (PI) approach based on the Moore-Penrose pseudo inverse using truncated singular value decomposition for regularization, which is robust to noise. It is shown that PI has an improved resolution of 24% over MF even at 0 dB SNR and is three orders of magnitude faster than the explicit inverse. A measurement based proof of concept experiment using a laboratory K-Band (15-26.5 GHz) ultra-wideband SAR system is shown to validate the proposed approach.

Index Terms— SAR, inverse problem, point spread function, truncated singular value decomposition (TSVD)

1. INTRODUCTION

Synthetic aperture radar (SAR) imaging was originally developed for reconnaissance and military use. The oldest form of SAR is stripmap mode SAR, where an airborne or space-borne radar platform moves along a trajectory while gathering measurements from a strip on the ground (see Fig. 1). The received signals are typically processed using 2-D correlation algorithms [1, 2]. However, SAR applications have evolved to more general radar imaging applications involving earth monitoring, remote sensing, surveillance, and security [3, 4, 5].

In general, SAR reconstruction algorithms can be classified into inverse filtering and migration methods [6]. Migration methods approximate the inverse by using the adjoint (e.g. matched filter), while inverse filtering methods explicitly find the inversion of the SAR forward model (e.g. a least squares solution). In [7], a comparison of different reconstruction algorithms including pseudo-inverse, matched filter, and iterative least squares are presented. It is shown that migration methods are more stable and robust to noise compared to inverse filtering, but the latter has improved resolution [6, 7]. When applying inverse filtering to SAR imaging, two additional critical challenges arise: inverse filtering is computationally costly in both memory and time, and the problem is often ill-posed [7, 8].

This paper proposes an algorithm to reduce the memory requirement of inverse filtering by partitioning the system model, solving the inverse for each part separately, and coherently integrating the solutions to reconstruct the final image. This so called partitioned inverse (PI) also allows for parallel processing. As many SAR problems are ill-posed, truncated singular value decomposition (TSVD) and L-curves [9] are proposed to regularize the partitioned sub-problems and to find the optimal truncation point.

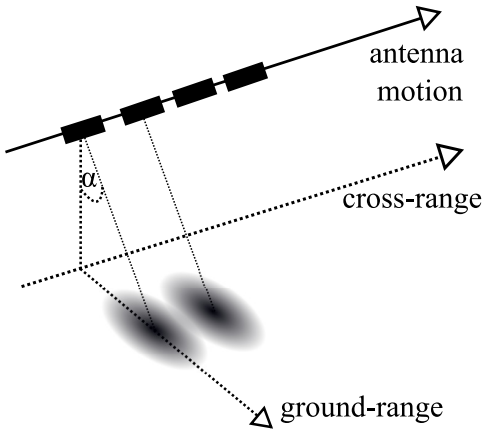

Fig. 1. Illustration of SAR Imaging System. The antenna is mounted on a moving platform. The antenna looking angle α is measured from the vertical axis.

The performance of the algorithm is analyzed using model resolution spread and point spread functions (PSF) as metrics. When truncating at 101 points, the model resolution spread improved by 2% and 1.3% using the proposed method vs. matched filter (MF) and full inverse (FI), respectively. PSFs under different noise levels are computed and it is shown that the PI approach is robust to noise and has better resolution than the MF, e.g. at 0 dB SNR the ground-range resolution has improved over MF by 24%. PI is highly efficient as it is three orders of magnitude faster than FI and, also shows improved computation time vs. MF. Experimental validation using a K-band (15-26.5 GHz) laboratory proof of concept apparatus are provided.

2. SYSTEM MODEL

SAR images are representations of the radar reflectivity of the observed scenes. As shown in Fig. 1, a radar antenna transmits a signal and receives the backscattered energy due to the illuminated point scatterers comprising the scene. This yields a position-dependent scene transfer function. Most SAR signals utilize wideband or ultra-wideband waveforms, as the ground-range resolution is inversely proportional to the bandwidth [10]. The cross-range (azimuth) resolution is inversely proportional to the length of the synthetic aper-

This work was partly supported by the United States Government. The published material represents the position of the authors and not necessarily that of the United States Government.

ture. Therefore, as the SAR platform moves, it measures transfer functions of the scene at different positions to create a large effective aperture [2]. At SAR system position $m \in \{1, \ldots, M\}$, the sampled frequency response vector $\mathbf{y}_m$ is measured. Assuming a scene consisting of N point scatterers, the received signal $y_{m,l}$, at the l-th frequency sample, where $l \in \{1, \ldots, L\}$, of the measurement vector $\mathbf{y}_m$ is

$$y_{m,l} = \sum_{n=1}^{N} a_{m,l,n} e^{-j\omega_l t_{m,n}} x_n + \nu_{m,l}, \tag{1}$$

where x_n is the complex reflection coefficient of the n-th point scatterer, $a_{m,l,n}$ is the path loss and antenna response, ω_l is the angular frequency, $t_{m,n}$ is the round-trip time delay between antenna position m and the n-th point scatterer, $\nu_{m,l}$ is measurement noise, and $j = \sqrt{-1}$. Concatenating all M measurements gives

$$\mathbf{y} = \mathbf{H}\mathbf{x} + \boldsymbol{\nu}, \tag{2}$$

where $\mathbf{y} = \left[\mathbf{y}_1^T \cdots \mathbf{y}_M^T\right]^T$ is the measurement vector, $\boldsymbol{\nu}$ is measurement noise, $\mathbf{x} = [x_1, \ldots, x_N]^T$ is the reflectivity vector of the point scatterers, and $(.)^T$ is the transpose operator. The measurement matrix $\mathbf{H}$ gives the dependence between the point scatterers and each measurement. The elements of the measurement matrix are defined as

$$[\mathbf{H}]_{m(L-1)+l,n} = a_{m,l,n} e^{-j\omega_l t_{m,n}}. \tag{3}$$

3. BASICS OF SAR IMAGE RECONSTRUCTION

SAR image reconstruction obtains an estimate of the reflection coefficients $\hat{\mathbf{x}}$ from the measurements by solving the inverse problem defined in (2), which can be formulated as

$$\hat{\mathbf{x}} = \mathbf{A}\mathbf{y}, \tag{4}$$

where $\mathbf{A}$ is the reconstruction matrix. In many cases $\mathbf{H}$ is not a full rank matrix and is therefore non invertible [7].

3.1. Model Resolution and Resolution Spread

The model resolution matrix $\mathbf{R}$ defines how well the model parameters can be resolved [11]. For a SAR system it defines how well the point scatterers can be resolved. Using (2) and (4), $\mathbf{R}$ is defined as

$$\mathbf{R} = \mathbf{A}\mathbf{H}. \tag{5}$$

Since the resolution matrix should ideally be an identity matrix $\mathbf{I}$, one possible measure is the spread of off-diagonal elements [11], where

$$\text{spread}\,\{\mathbf{R}\} = ||\mathbf{R} - \mathbf{I}||_2^2 = \sum_{i=1}^{N}\sum_{j=1}^{N}[[\mathbf{R}]_{i,j} - [\mathbf{I}]_{i,j}]^2. \tag{6}$$

3.2. Reconstruction using Matched Filter

The MF is a migration method where the inverse is approximated by the adjoint operator, thus,

$$\mathbf{A} = \mathbf{H}^*, \tag{7}$$

where $(.)^*$ is the complex conjugate transpose operator. For the MF, the resolution matrix is obtained as $\mathbf{R}_{\text{MF}} = \mathbf{H}^*\mathbf{H}$. However, as the inverse is approximated, the achievable resolution is limited [6].

3.3. Reconstruction using Inverse Filtering

The Moore-Penrose pseudo inverse $\mathbf{H}^\dagger$ provides a least-squares solution to the system model [8]. The least squares solution is an inverse filtering method given as

$$\mathbf{A} = \mathbf{H}^\dagger. \tag{8}$$

Here $\mathbf{R}_{\text{FI}} = \mathbf{H}^\dagger\mathbf{H}$, and in an overdetermined least squares problem ($ML > N$), $\mathbf{R}_{\text{FI}}$ is an identity matrix [11].

The Moore-Penrose pseudo inverse can be computed using singular value decomposition (SVD). A bad condition number, indicating that there exist singular values that are small compared to the rest, causes the inverse to be unstable and the problem to be ill-conditioned. Furthermore, the computation of the pseudo inverse is computationally complex. $\mathbf{H}$ gives the relationship between all the point scatterers and all the elements in the measurement vector. Thus it is a large matrix and computing the full inverse requires a lot of memory. In many cases this approach is impractical given the hardware constraints of standard PCs.

4. PARTITIONING OF THE INVERSE PROBLEM

A possible solution to handle the computational hardware constraints and a large set of data is to partition the inverse problem. The partitioning is two-fold: 1) partitioning of the measurement vector into sub-apertures $\{\mathbf{y}_m\}$ by the SAR system position, and 2) partitioning the reconstruction scene as observed by the 3 dB beamwidth of the antenna at each position. Note that contributions of point scatterers outside of the 3 dB antenna beamwidth are not considered in the forward model. Although this inevitably results in model residuals, simulations and validation measurements (as presented here) suggest that this error is insignificant and can be neglected. Hence, a possible partition of the scene is

$$\tilde{\mathbf{x}}_m = [x_{m,1}, \ldots, x_{m,N'}]^T, \tag{9}$$

where $N' << N$ is the number of point scatterers observed by the antenna at each position. The model for partition m is given as

$$\mathbf{y}_m = \mathbf{H}_m\tilde{\mathbf{x}}_m + \boldsymbol{\nu}_m. \tag{10}$$

$\mathbf{H}_m$ is a $L \times N'$ matrix, which is much smaller than the size of the original $(ML) \times N$ measurement matrix. Instead of obtaining the inverse of the full measurement matrix, this approach computes the inverse of the sub-measurement matrices and solves for each sub-aperture separately.

An added advantage of such a partition is that the sub-measurement matrix $\mathbf{H}_m$ is constant for all the partitions in the stripmap mode. Defining $\mathbf{H}_{\text{s}}$ as the constant sub-measurement matrix, $\mathbf{H}_m = \mathbf{H}_{\text{s}}\ \forall\ m \in \{1, \ldots, M\}$. As of (3), the variables in the measurement matrix are the frequencies $\{\omega_l\}$ and time delays $\{t_{m,n}\}$. The frequency samples remain the same for each system position, and by fixing the reconstruction scene for each position the time delays also remain constant. Therefore, construction of the sub-measurement matrix and the inversion needs to be done only once. This potentially saves a lot of memory and computation time.

As the measurements and reconstruction points are partitioned for each SAR position, the system model can be rearranged to give

$$\mathbf{y} = \tilde{\mathbf{H}}\tilde{\mathbf{x}} + \boldsymbol{\nu}, \tag{11}$$

where $\tilde{\mathbf{x}} = [\tilde{\mathbf{x}}_1^T \cdots \tilde{\mathbf{x}}_M^T]^T$, and the rearranged measurement matrix

$$\tilde{\mathbf{H}} = \begin{bmatrix} \mathbf{H}_s & \mathbf{0} & \cdots \\ \mathbf{0} & \ddots & \\ \vdots & & \end{bmatrix} \tag{12}$$

being a block diagonal matrix. The inverse is given as

$$\hat{\mathbf{x}} = \mathbf{W}\tilde{\mathbf{H}}^{\dagger}\mathbf{y}, \tag{13}$$

where $\mathbf{W}$ is a weighted summation matrix which sums up any contributions of the components $\{\hat{x}_n\}$ in the vector $\tilde{\mathbf{H}}^{\dagger}\mathbf{y}$, and $\tilde{\mathbf{H}}^{\dagger}$ is defined as

$$\tilde{\mathbf{H}}^{\dagger} = \begin{bmatrix} \mathbf{H}_s^{\dagger} & \mathbf{0} & \cdots \\ \mathbf{0} & \ddots & \\ \vdots & & \end{bmatrix}. \tag{14}$$

Here, the resolution matrix is $\mathbf{R}_{\mathrm{PI}} = \mathbf{W}\tilde{\mathbf{H}}^{\dagger}\tilde{\mathbf{H}}$. The matrix $[\tilde{\mathbf{H}}^{\dagger}\tilde{\mathbf{H}}]$ is a block diagonal matrix with the elements being $\mathbf{H}_s^{\dagger}\mathbf{H}_s$. Hence, as with the full inverse, $\mathbf{R}_{\mathrm{PI}}$ will be an identity matrix for overdetermined systems ($L > N'$).

For most cases $\mathbf{H}_s$ is ill conditioned and needs to be regularized. A possible regularization, which is used in this work, is truncated singular value decomposition (TSVD) [8]. In TSVD, small singular values are discarded and only the strongest singular values are kept. Thus, if more singular values are kept the resolution will improve, but if some singular values are small compared to the rest, the system will be unstable and more sensitive to noise. If only a low number of singular values are kept, noise can be mitigated, but information will be lost in the process (yielding regularization errors [9]). Hence, an optimal truncation point needs to be found.

There are several methods proposed in the literature to find the optimal truncation point. These include unbiased predictive risk estimator, discrepancy principle, generalized cross validation, and the L-curve method [8]. In this work the L-curve method is used as it is more robust in the presence of correlated errors and does not need prior information about the errors. The L-curve is a parametric plot of the norm of the regularized solution $\hat{\mathbf{x}}$ versus the norm of the corresponding residual $\mathbf{H}\hat{\mathbf{x}} - \mathbf{y}$ [9]. The corner of the L-curve corresponds to a good balance between minimization of the sizes, and the corresponding residuals. At this point the solution changes from being dominated by regularization errors to being dominated by noise. Assuming measurement noise remains constant across all positions, the optimal truncation needs to be found only once, as it can be used for all sub-partitions.

5. PERFORMANCE ANALYSIS

In this section, results based on synthesized data for FI, MF and PI are presented. The simulation setup assumes a horn antenna with a half power beam width of 58°. The antenna is moved over 0.10 m at intervals of 4 mm, with a looking angle of 30° and a platform height of 0.3 m. Frequencies from 20 GHz to 26 GHz are used with a sampling interval of 60 MHz (101 values). The scene to be reconstructed is 0.2 m in ground-range and 0.484 m in cross-range. These values were chosen to make reconstruction using FI possible on the workstation used to prepare this paper (Intel core i7-6700 CPU at 3.4 GHz with 16 GB memory).

In Fig. 2, a comparison of the model resolution spread (see (6)) for FI, MF and PI is shown. The values are normalized using the

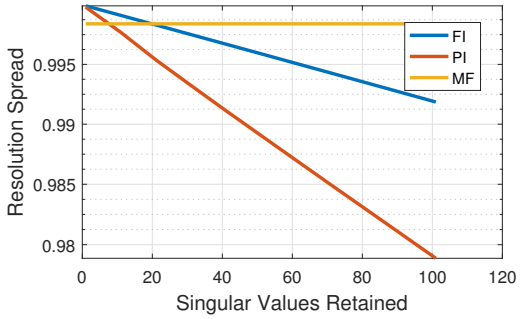

Fig. 2. Model resolution spread plotted as a function of number of singular values retained.

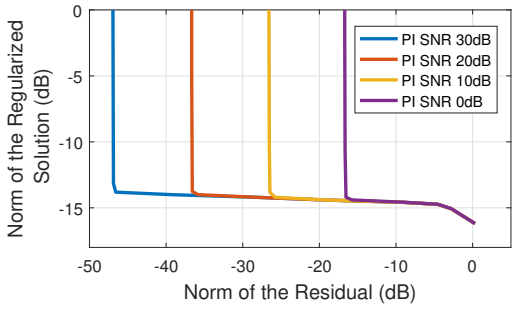

Fig. 3. L-curves plotted for different noise levels.

norm of $\mathbf{I}$. The maximum number of singular values retained is 101, as that is the minimum size of $\mathbf{H}_s$. The resolution spread of FI and PI changes with the amount of truncation, and at 101 points it is 0.9919 and 0.9789 respectively. The resolution spread of MF is 0.9984, and is near the lower bound of both FI and PI. There is an improvement of 2% and 1.3% in the resolution spread in PI over MF and FI respectively, at 101 points.

For PI, the number of reconstruction points is much less than for FI. Therefore, when a small number of singular values are kept, $\mathbf{R}$ is higher for PI than for FI. Furthermore, in PI only the points in the partitioned scene affects the estimate and most of the off diagonal elements in $\mathbf{R}$ are zero.

In Fig. 3, L-curves for PI with various SNR values are shown. The corner points of the L curves represent the optimal truncation point for the respective noise levels; 30 dB SNR: 17 points, 20 dB SNR: 15 points, 10 dB SNR: 13 points and 0 dB SNR: 11 points. As the noise level increases, the norm of the residual also increases.

Figures 4a-4b demonstrate the effect of different noise levels for a PSF with a fixed truncation of 15 points. For signals with 0 dB and 10 dB SNR, the point scatterer is not resolvable. For signals with lower noise levels, the resolution of the PSF is 1.87 cm in ground-range and 2.38 cm in cross-range, which remains the same as the truncation point is fixed.

PSFs using optimal truncation points for different noise levels are shown in Figs. 4c-4d. As the resolution depends on the amount of truncation, for different noise levels different resolutions can be observed. In an ideal case with no noise, the PSF is a peak as there is no truncation. When the noise level increases the resolution degrades. This is clearly visible in Fig. 4c, with the ground-range resolution for respective noise levels being, 0 dB SNR: 2.36 cm, 10 dB SNR: 2.09 cm, 20 dB SNR: 1.86 cm, and 30 dB SNR: 1.69 cm.

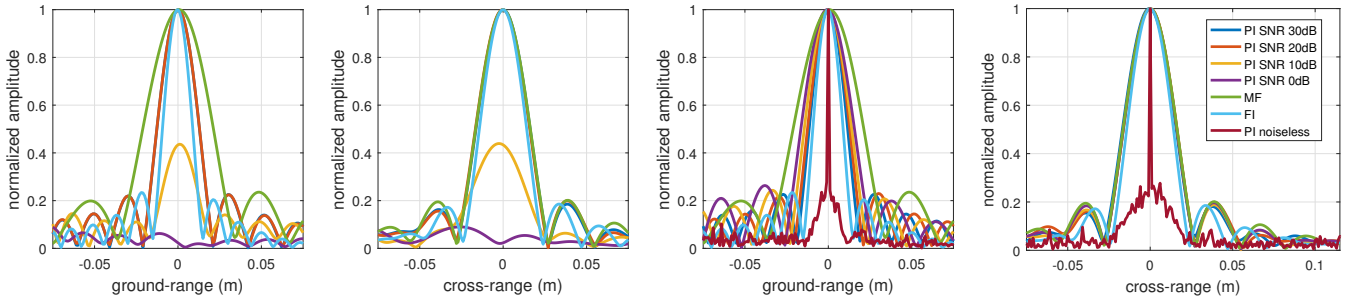

(a) (b) (c) (d)

Fig. 4. Effect of noise: (a) ground-range profile of the PSF with a fixed truncation, (b) cross-range profile of the PSF with a fixed truncation, (c) ground-range profile of the PSF with optimal truncation, (d) cross-range profile of the PSF with optimal truncation.

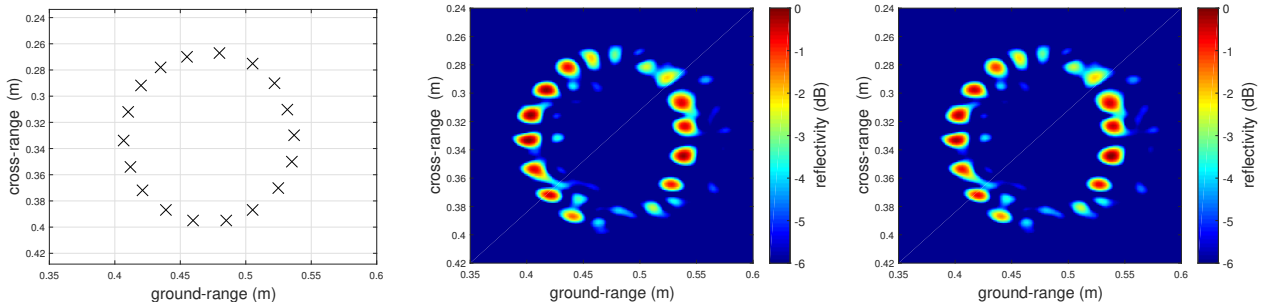

(a) scene (b) MF (c) PI

Fig. 5. Experimental results: (a) positions of point targets, (b) MF reconstruction, (c) reconstruction using PI (36 singular values retained).

However, as the cross-range data is limited, a resolution degradation is not visible in Fig. 4d. The cross-range resolution is 2.38 cm across all noise levels, which suggests that the PI method is robust to noise.

For comparison, the PSF with MF and FI under ideal conditions are shown in Figs. 4a-4d. Resolution with MF is 3.10 cm in ground-range and 2.40 cm in cross-range, while resolution with FI is 1.33 cm and 2.07 cm respectively. When computing the FI, the default truncation level computed by *Matlab* (506) was used, and thus a good resolution was achieved. However, even for 0 dB SNR, the resolution has improved by 24% in ground-range and by 0.83% in cross-range for PI over MF.

For a reconstruction of the PSF, PI took 1.9 s, MF 7.2 s and FI 2200 s, making PI 1200 times faster than FI and 4 times faster than MF.

6. MEASUREMENT-BASED VALIDATION

In this section, experimental results using a Pasternack PE9852/2F-10 K-band horn antenna with a half power beam width of 58° are presented. The antenna is moved 0.57 m at a spacing of 4 mm and a looking angle of 60° on a platform at a height of 0.3 m. Frequencies from 15 GHz to 26.5 GHz are used, spaced at 50 MHz intervals. At each antenna position, transfer function measurements are collected using an Agilent A5222N vector network analyzer. The reconstruction scene is 0.6 m in ground-range and 1.1 m in cross-range. The cross-range was chosen to reconstruct the scene as observed by all antenna positions. The spacing between voxels is 1 mm. A circle of point scatterers consisting of eighteen 1/4"–20 nuts comprises the scene to be imaged. The nuts were placed equidistantly on a circle of 13 cm in diameter.

Reconstructed images using MF and PI are shown in Figs. 5b-5c, respectively, where reflectivity is normalized and represented on a log scale. Reconstruction using FI was not possible with the available 16 GB of memory. The MF and PI images show essentially no visible difference. This suggests that PI works amidst real measurement noise. Reconstruction using MF took 230 s while PI took only 29 s, making PI 8 times faster on our workstation.

7. CONCLUSION

In this work a partitioned inverse (PI) solution for reconstructing SAR images was presented which is computationally more efficient than the full inverse (FI). On our test problems, PI was three orders of magnitude faster than FI. It was shown that truncated singular value decomposition is a possible regularizer for the proposed algorithm. It was also shown that the PI can achieve better resolution than the matched filter (MF) and is robust to noise with optimal regularization. With 0 dB SNR, the resolution using PI improved vs. MF by 24% in ground-range and by 0.83% in cross range. Furthermore, the PI reconstruction time was shorter than with MF. Experimental results that validated the algorithm with measurement noise were shown. PI has promise as an alternative inverse filtering method for SAR which avoids the time and memory constrains of the full inverse, while maintaining improved resolution.

8. REFERENCES

[1] D. C. Munson and R. L. Visentin, "A signal processing view of strip-mapping synthetic aperture radar," *IEEE Transactions on Acoustics, Speech, and Signal Processing*, vol. 37, no. 12, pp. 2131 – 2147, December 1989.

[2] I. G. Cumming and F. H. Wong, *Digital Processing of Synthetic Aperture Radar Data: Algorithms and Implementation*, Artech House, 2005.

[3] R. Appleby and R. N. Anderton, "Millimeter-wave and submillimeter-wave imaging for security and surveillance," *Proceedings of the IEEE*, vol. 95, no. 8, pp. 1683–1690, Aug 2007.

[4] D. M. Sheen, D. L. McMakin, and T. E. Hall, "Three-dimensional millimeter-wave imaging for concealed weapon detection," *IEEE Transactions on Microwave Theory and Techniques*, vol. 49, no. 9, pp. 1581–1592, Sep 2001.

[5] J. Hunt, J. Gollub, T. Driscoll, G. Lipworth, A. Mrozack, M. S. Reynolds, D. J. Brady, and D. R. Smith, "Metamaterial microwave holographic imaging system," *J. Opt. Soc. Am. A*, vol. 31, no. 10, pp. 2109–2119, Oct 2014.

[6] R. Solimene, I. Catapano, G. Gennarelli, A. Cuccaro, A. Dell'Aversano, and F. Soldovieri, "SAR imaging algorithms and some unconventional applications: A unified mathematical overview," *IEEE Signal Processing Magazine*, vol. 31, no. 4, pp. 90 : 98, July 2014.

[7] O. Yurduseven, J. Gollub, H. Odabasi, M. F. Imani, G. Lipworth, A. Rose, P. Trofetter, and D. R. Smith, "Comparison of different reconstruction algorithms for image reconstruction in metamaterial aperture based imaging system," *European Conference on Antennas and Propagation*, January 2015.

[8] C. R. Vogel, *Computational Methods for Inverse Problems*, Society for Industrial and Applied Mathematics, Philadelphia, 2002.

[9] P. C. Hansen and D. P. O'Leary, "The use of the L-curve in the regularization of discrete ill-posed problems," *SIAM Journal on Scientific Computing*, vol. 14, no. 6, pp. 1487:1503, 1993.

[10] A. Moreira, P. Prats-Iraola, M. Younis, G. K. I. Hajnsek, and K. P. Papathanassiou, "A tutorial on synthetic aperture radar," *IEEE Geoscience and Remote Sensing Magazine*, vol. 1, no. 1, pp. 6:43, March 2013.

[11] W. Meneke, *Geophysical Data Analysis:Discrete Inverse Theory*, International Geophysics Series, Academic Press, London, 1984.